

Research Article

Deep Learning-Based Wildfire Image Detection and Classification Systems for Controlling Biomass

M. Prakash ¹, S. Neelakandan,² M. Tamilselvi,³ S. Velmurugan,⁴ S. Baghavathi Priya ⁵,
and Eric Ofori Martinson ⁶

¹School of Computer Science and Engineering, Vellore Institute of Technology, Vellore, India

²Department of Computer Science and Engineering, RMK Engineering College, Chennai, India

³Information Technology Department, University of Technology and Applied Sciences, Nizwa, Oman

⁴Department of Information Technology, R.M.D. Engineering College, Kavaraipettai, Tamil Nadu 601206, India

⁵Department of Computer Science and Engineering, Amrita School of Computing, Amrita Vishwa Vidyapeetham, Chennai, India

⁶Department of Electronics and Communication Engineering, All Nations University, Koforidua, Ghana

Correspondence should be addressed to Eric Ofori Martinson; emartinson@anuc.edu.gh

Received 25 March 2023; Revised 23 June 2023; Accepted 8 September 2023; Published 16 September 2023

Academic Editor: Alexander Hošovský

Copyright © 2023 M. Prakash et al. This is an open access article distributed under the Creative Commons Attribution License, which permits unrestricted use, distribution, and reproduction in any medium, provided the original work is properly cited.

Forests are essential natural resources that directly impact the ecosystem. However, the rising frequency of forest fires due to natural and artificial climate change has become a critical issue. A revolutionary municipal application proposes deploying an artificial intelligence-based forest fire warning system to prevent major disasters. This work aims to present an overview of vision-based methods for detecting and categorizing forest fires. The study employs a forest fire detection dataset to address the classification difficulty of discriminating between photos with and without fire. This method is based on convolutional neural network transfer learning with Inception-v3. Thus, automatic identification of current forest fires (including burning biomass) is a critical field of research for reducing negative repercussions. Early fire detection can also assist decision-makers in developing mitigation and extinguishment strategies. Radial basis function Networks (RBFNs) with rapid and accurate image super resolution (RAISR) is a deep learning framework trained on an input dataset to detect active fires and burning biomass. The proposed RBFN-RAISR model's performance in recognizing fires and nonfires was compared to earlier CNN models using several performance criteria. The water wave optimization technique is used for image feature selection, noise and blurring reduction, image improvement and restoration, and image enhancement and restoration. When classifying fire and no-fire photos, the proposed RBFN-RAISR fire detection approach achieves 97.55% accuracy, 93.33% F-Score, 96.44% recall, 94.19% precision, and an error rate of 24.89. Given the one-of-a-kind forest fire detection dataset, the suggested method achieves promising results for the forest fire categorization problem.

1. Introduction

Forests are necessary for the supply of minerals and other industrial components. Forests aid the ecology by providing a home for species and removing carbon dioxide from the air. Forests can stop sandstorms, protecting the environment and agriculture. Climate change has increased the frequency of forest fires [1]. Hot, dry weather causes wildfires, which damage not just the environment but also humans, animals, and the ecology. Coniferous trees produce more flammable

sap than deciduous trees. Conifers have thicker growth than other tree species, which makes them more explosive. Fires damage millions of acres of forest annually, causing economic losses. Brazil, Australia, America, and Canada have all experienced devastating forest fires [2, 3].

A severe fire in Australia in 2020 destroyed many homes, businesses, forests, and people. The fire damaged 1500 homes, killed almost a quarter-million animals, and took the lives of 23 people [4, 5]. Terrible wildfires ravaged California's woods and the Amazon rainforest in 2018 and 2019

[6, 7]. Between 1992 and 2015, people started 85% of the forest fires in the United States, while just 15% were brought on by lightning or climate change. This forest fire might have been prevented if locals had decreased their activity level. Since the COVID-19 outbreak started, there have been fewer forest fires. Many nations implemented complete lockdowns during this period [8]. Early fire detection significantly decreases the risk of devastating forest fires because it gives firefighters more time and resources to put out the fire while it is still tiny. The ability to better regulate fire exists [9].

Governments worldwide are developing sophisticated surveillance and fire detection systems to avoid burning forests. Prompt detection and communication by authorities can help lessen forest fire dangers. This factor reduces the risk of forest fires and influences the precision of human monitoring. IoT uses wireless networks, cloud storage, and sensors in smart cities. The Internet of Things enables us to link our intelligent devices. IoT devices generate a plethora of data that AI systems can process. Because of the massive amounts of data generated, computer vision has become a valuable tool for intelligent monitoring [10].

Deep or traditional machine learning can identify fires in images and videos [11]. It works in both directions [12]. In the past, feature extraction and selection processes were required to optimize machine learning performance. Deep learning automatically selects and extracts features for classification [13]. Adopting the method is beneficial. Manual feature extraction cannot produce discriminative feature information when dealing with extensive data. Handcrafted methods are untrustworthy because they perform poorly in classification tasks with larger datasets. Deep learning approaches can handle enormous volumes of data, but they need to consider the complexity of the training sample. As a result, the model's performance suffers, as does the effectiveness of their training models. Deep learning is less effective in complex fire scenarios with few data and characteristics. In the current study, higher-order visual features were extracted using machine learning to distinguish between fire and nonfire pixels.

When used as activation functions, radial basis functions (RBFs) differentiate radial basis function networks (RBFNs), a subclass of feedforward neural networks and universal approximators, from other classes of neural networks. RBFN is commonly used in regression, classification, pattern recognition, and time series forecasting [14]. RBFNs excel at simulating the real world, as well as in a variety of other areas. These features include resistance to background noise, the ability to affect any continuous network, and a small environmental footprint. The current techniques have produced promising results, which localize wildfires and identify the specific geometry of fires using input photos obtained from conventional visual sensors. Despite the various difficulties that could arise, like the small size of the objects, the complicated background, and possible image degradation, the efficiency of these techniques for recognizing and isolating forest fires through pixel photos still needs to be discovered.

To increase the accuracy of fire detection, an Inception-v3 model based on CNN is being used in this work. This

model classifies satellite photos into fire and nonfire images and trains satellite images using datasets. Therefore, the automated identification of active forest fires (together with burning biomass) holds tremendous significance as a study domain to reduce unfavorable effects. Making decisions early on can assist decision-makers in planning mitigation and extinguishment strategies. RBFN with RAISR is a deep learning framework trained on an input dataset to detect active fires and burning biomass. The proposed RBFN-RAISR model's performance in recognizing fires and nonfires was evaluated using a variety of performance metrics and compared to previous CNN models. The water wave optimization technique is used for effective picture feature selection, image noise, blurring reduction, and image enhancement and restoration. Given an image, we want to create a larger image with much more pixels and better image quality. This is sometimes called the single image super-resolution (SISR) problem. The idea is that with enough training data (corresponding pairs of low- and high-resolution images), we can learn a set of filters (i.e., a mapping) that, when applied to a given image that is not in the training set, will produce a higher-resolution version of it, preferably with low-complexity learning. Our suggested solution has a runtime that is one to two orders of magnitude faster than the top rivals now on the market while still generating results that are on par with or better than state-of-the-art. The benefits of this study are as follows:

- (i) The research on forest and wildland fire localization and classification algorithms based on computer vision will be discussed.
- (ii) The use of our freshly curated dataset for this study greatly improves the accuracy of fire identification by differentiating between images showing fire and those without fire in the dataset for detecting forest fires. Our research is entirely focused on forest fires, as opposed to earlier wildfire studies that covered a variety of landscapes, including wildlands, shrubs, and farmlands.
- (iii) Introduce Inception-v3, a convolutional neural network (CNN)-based transfer-learning strategy, developed for the classification of forest fires using a regional dataset. To evaluate the MobileNetV2 model, this approach utilizes the learned weights of the fully connected layer and the convolutional base layer to complete complex feature learning and classification tasks.
- (iv) Compare, using alternative CNN models on the dataset for forest fires, the outcomes of the proposed RBFN-RAISR technique with various performance criteria.

The project is structured as follows: The second section covers the theory that guides everything in more detail. The proposed system's framework will be the main topic of Section 3. Section 4 presents our report containing a description of our experiments. A summary is found in Section 5.

2. Literature Survey

Early wildfire identification by UAVs employing deep-learning computer vision techniques was studied by Bouguettaya et al. [15]. The existing literature on smoke or fire detection classifies and differentiates detection methods. White pixels represent fire dispersion in the latter, while the remaining pixels serve as the background to generate a mask using pixel-based clustering. For segmentation-based deep learning, a powerful GPU is required. Make photographs as small as possible before feeding them to deep-learning models. It can be challenging to identify specific fire pixels in some aerial pictures. Because of the dimensionality of these images, training data may be different, which can affect classification results. Sliding windows will scan the original photographs and sort them into several categories. The model will include flame and smoke windows. For the first task, multiple classifiers are used.

Cao et al. [16] proposed categorizing forest fire smoke using a novel classification system. This novel technique is called “attention-enhanced bidirectional long-short-term memory.” The attention network optimizes classification within this framework, while Inception-v3 extracts spatial features and Bi-LSTM extracts temporal data. Sousa et al. [17] developed a transfer-learning strategy for identifying wildfires. Its designers previously trained the model weights to recognize fires. This was part of their strategy.

Alexandrov et al. [18] compared CNN and machine learning algorithms to spot forest fires. The accuracy of detection was assessed by the authors using their dataset. Zhang et al. [19] suggested a CNN-based fire detector. The proposed method classifies images using SVM and transfers learning from AlexNet. After the data has been classified, the hotspot is discovered using pooling-5 and a fine-grained patch classifier. Patch localization outperformed complete image classification in fire detection accuracy.

Yar et al. [20] introduced that the dual fire attention network will help achieve accurate and effective fire detection with a reasonable trade-off between computational cost and accuracy. The initial attention approach produces significantly emphasized feature maps by highlighting the most appropriate channels from the characteristics of an existing backbone model. Then, a modified spatial attention mechanism is employed to gather spatial data and improve discrimination between items on fire and those not. By reducing many unnecessary factors from the DFAN using a meta-heuristic method, we further improve it for practical applications, resulting in FPS values that are about 50% higher.

Saydirasulovich et al. [21] examined how well YOLOv6, an NVIDIA GPU-based object identifier, could distinguish between different fire-related objects. We analyzed the effect that YOLOv6 had on fire detection and identification in Korea using several measures, including object recognition speed, accuracy studies, and time-sensitive real-world applications. To evaluate YOLOv6’s fire recognition and detection capabilities, we amassed a dataset of 4,000 images from diverse sources, including Google and YouTube. The results showed that YOLOv6 had a precision of 0.83, an

average recall of 0.96, and an item identification performance of 0.98. There is a mean absolute error of 0.302% in the system.

Yar et al. [22] created an advanced method that uses a lightweight convolutional neural network (CNN) that is compatible with low-powered devices. The suggested model’s underlying architecture is based on the block-wise VGG16 architecture; however, it achieves substantially improved accuracy in early fire detection with fewer parameters, a smaller input size, and a shorter inference period. The model employs small-size uniform convolutional filters with increasing channel capacity, allowing for more effective feature extraction. These filters excel at extracting even the smallest features from the fire photos provided as input. Experiments were carried out on two datasets to test the model’s performance: the internationally recognised Foggia’s benchmark dataset and a freshly generated, demanding real-world fire detection dataset.

Big data, remote sensing, and data mining approaches were employed by Sayad et al. [23] to forecast wildfires. Three crop-related factors were used to create a dataset using preprocessed MODIS data. Thermal anomalies, LST, and NDVI were the parameters. To predict wildfires, two supervised classification techniques were used. The SVM method achieved 97.48% accuracy, while the neural network method achieved 98.32%. The model’s predictive power for wildfires was investigated and evaluated using classification metrics, cross-validation, and regularization.

Khan et al. [24] introduced the Stacked Encoded-EfficientNet (SE-EFFNet), a deep model aiming to optimise cost while obtaining lower false alarm rates and increased fire identification capabilities. SE-EFFNet builds on the lightweight EfficientNet, capturing valuable features that are then reinforced with stacked autoencoders before arriving at the final classification. To solve the issues associated with vanishing gradients, SE-EFFNet combines dense connections with randomly initialised weights, ensuring rapid convergence speed.

Zhang et al. [25] employed synthetic smoke images to create a quicker R-CNN for forest smoke detection. Nature Communications published an explanation of their procedure. To identify SroFs and nonfire zones, the researchers used a faster R-CNN to retrieve spatial information. The features of the identified SroFs were stored in a long-short-term memory in a series of frames to determine whether there was a fire swiftly. The decision was made using a majority vote and the principles of fire dynamics.

The comparative study of various surveys of forest fire image detection and classification is disclosed in Table 1.

According to the study above, CNNs have considerable promise for fire detection. They can help establish a reliable system that significantly decreases both human and financial losses from fires. Our literature analysis revealed that while research on detecting forest fires and smoke from photographs has been conducted, no work has been done on the forgetting phenomenon that occurs when trained models are used for new tasks involving fire and smoke images. The use of CNN for fire and smoke detection still

TABLE 1: Survey of forest fire image detection and classification.

Research	Title	Method	Accuracy	Classes	Year
Khan et al. [26]	Deep transfer learning for forest fire detection: A new dataset and performance benchmark	VGG19	95.0%	Fire and no-fire	2022
Park et al. [27]	Deep transfer learning for decision-supporting multilabel image classification in wildfire situations	VGG16, ResNet50, Densenet121	—	Fires, nonfires, flames, smoke, structures, and people	2021
Kaabi et al. [28]	In a video of a forest fire, the first smoke was found using a deep belief network	DBN	95%	Smoke and no smoke	2018
Sousa et al. [17]	Using enhanced datasets with transfer learning to detect fires	Inception-v3	93.6%	Fire and not fire	2019
Tang et al. [29]	Deep learning in a forest environment for image classification	ForestResNet	92%	Normal, smoke and fire	2021
Alexandrov et al. [18]	Deep learning in a forest environment for image classification	HaaR, LBP, YOLOv2, Faster R-CNN, SSD	87.4%, 81.3%, 98.3%, 95.9%, 81.1%	Smoke and forest background	2019
Li and Yu [30]	An efficient convolutional neural network algorithm for detecting fire	Yolo-edge	—	Nonforest fires and forest fires	2021

has several critical drawbacks, including the need for faster training, improved parameter efficiency, hyperparameter tweaking, and transfer learning across new datasets. None of the abovementioned investigations attempted to adjust the hyperparameters, although transfer learning was employed in a few trials to speed up the training process. In conclusion, using a combination of deep understanding, transfer learning, and hyperparameter tuning, we create a few classification models that can distinguish between fire and smoke in photographs. This process saves time and ensures early detection.

3. Proposed System

3.1. Forest Fire Detection System. Detecting forest fires is particularly challenging in remote areas, such as highland woods. This makes flame detection difficult. The atmospheric and meteorological conditions are also volatile. These elements impact the development of algorithms for early forest fire detection. We provide a deep learning-based approach to categorize forest fires for applications in AI-powered intelligent cities. This natural treasure is protected by looking for fires while in the forest. The RBFN model uses forest images to determine whether or not a fire is present. Ad hoc networks and cloud computing can send fire information to a remote forest fire response center. This study categorizes forest fires to identify RBFN accurately. The method of informing and connecting the outlying fire station is an integral part of this program. The proposed method's architecture is shown in Figure 1.

A distant forest monitoring center receives real-time information about forest fires using the suggested RBFN methodology as a resource-constrained forest fire fighting system method. The recommended RBFN strategy will build a network of cooperation and ad hoc communication, conserving the limited battery resources and minimizing the wait time while using other intermediary mediums like satellites.

Detecting forest fires is inherently challenging since reaching remote areas like highland woods is challenging. Furthermore, these locations have a volatile environment with changing air quality. An automated system for the early identification of forest fires relies significantly on these features. Therefore, machine learning algorithms need a lot of data to get good at detecting things. Several machine learning methods exist for the task of classifying forest fires. We also recommend the Inception-v3-based transfer-learning approach for a successful forest fire warning system to improve classification prediction accuracy.

3.2. Dataset. The most recent literature contains information about wildfires. This dataset contains images of various subjects, including cityscapes and forest fires. Given that forest fires are the subject of the current inquiry, we decided to leverage our forest fire dataset to help develop fresh strategies that might be applied in the future to deal with this issue. More information can be found at [31], where the dataset is also available.

On-site information about forest fires was made available by the Korea Forest Service (<https://www.forest.go.kr>) through visits by regional public experts. This information included specifics like the beginning and ending times of the fires, their locations, the size of the impacted areas, and the reasons why they occurred. Only forest fires reported by Jang et al. [32] between October 2015 and December 2019 were considered for this analysis. These fires were chosen because they exceeded the requirement of 0.7 hectares in damage and had no cloud interference. Finally, 91 forest fire incidences in all were used as reference data. Seven of these occurrences fell into the category of large forest fires, with damage areas over 100 hectares, while 16 cases fell into the category of small forest fires, with damage areas under 1 hectare.

3.3. Preprocessing. We utilized various editing techniques to enhance the quality of the photos we had shot, including random rotation, vertical and horizontal flipping, and labeling. The first sign of impending peril was the development of an irregularly shaped cloud of smoke. Unlike objects with a constant shape, such as people and cars, smoke can flow in many directions and take various forms. Because smoke lacks a predetermined condition, picture augmentation can be successfully applied to the objective of training data augmentation. The distribution of the training dataset was not uniform across all classes, which was the second issue. The method in which the number of instances is spread among the ranks is shown graphically in Figure 2. Depending on the category under investigation, a varying number of cases of image enhancement were applied. As a result, we could identify a remedy for the issue. The use of picture augmentation in such a way as to increase the model's detectability to a more reasonable level is strongly advised.

3.4. Dataset Distribution. There are 950 photos in the collection that have been recognized as being from the fire instance. In contrast, the no-Ffire model is recognized in the remaining 950 photos. Twenty percent of the data was used for testing, while 80 percent was used for training. Specifically, the movement used 80% of the training data, and validation used 20%. Table 2 depicts the partitioning of data for use in training and testing [33].

3.5. Augmentation of Data. The dataset for forest fires contains a variety of photographic styles. The trained model may not generalize well to new data because the dataset needs to reflect a wide range of images sufficiently. We expanded the training dataset by enlarging, flipping, moving, zooming, and other techniques. Before introducing the model, we reduced the image sizes in both classes to 224 by 224 pixels, the MobileNetV2 model's minimum input size. Table 3 describes improved datasets [34].

3.6. Radial Basis Function Network. The perimeter of a wildfire can be viewed as a collection of dispersed points $\Gamma(s)$. The level set algorithm defines the fire boundary as

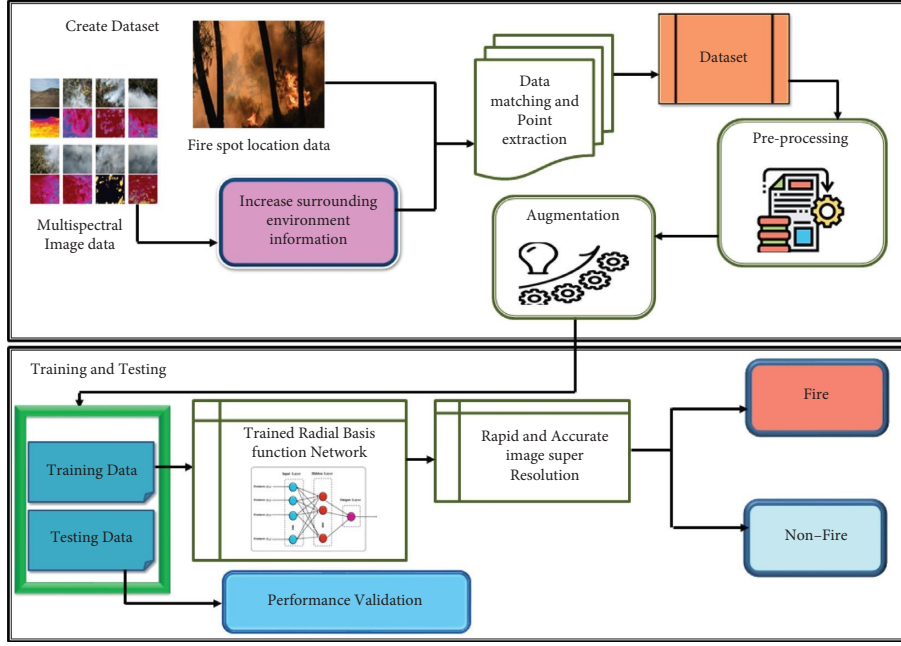


FIGURE 1: Proposed method of RBFN-RAISR.

a zero-level set of a smooth time-dependent function. The level set algorithm's operation enables this $\Phi(y, s): \mathbb{R}^2 \rightarrow \mathbb{R}$, namely,

$$\Gamma(s) = \{y \in \mathbb{R}^2 \mid \Phi(y, s) = 0\}. \quad (1)$$

Typically, the signed distance function provided is used to initialize Φ .

$$\Phi(y, 0) = \begin{cases} -d_{\Gamma(s)}(y), & y \text{ inside the fire boundary,} \\ 0, & y \text{ on the fire boundary,} \\ d_{\Gamma(s)}(y), & y \text{ outside the fire boundary,} \end{cases} \quad (2)$$

where $d_{\Gamma(s)}(y)$ is the distance between x and the nearest place on the wildfire boundary in [35]. Figure 3 shows how RBFN is structured.

RBFNs are axially symmetric functions with actual values. In other words, value is determined by distance from the center. Because of its simplicity, ease of implementation, and good approximation behavior, the radial basis function approach is a popular alternative when generating a geometric model from multivariate scattered data. It is a reliable approximation. Thin-plate splines and other radial-based functions are used in this study to create wildfire boundary conditions. Many activities emanate from the center. Spline notation for thin plate:

$$g_i(y) = \|y - y_i\|^2 \log(\|y - y_i\| + 1), \quad (3)$$

where the terms being discussed here are the radial basis function center. $\|\cdot\|$ specifies the operator that denotes the Euclidean norm. One can estimate the spots on the wildfire boundary using N thin-plate splines with N fixed centers. This could be represented, for example, by

$$\Phi(y, s) = \sum_{i=1}^N \lambda_i(s) g_i(y) + p(y, s), \quad (4)$$

where coefficients $\lambda_i(s)$ are real numbers and $p(y, s)$ is a first-order polynomial that has been modified over time to account for the linear and constant portion of $\Phi(y, s)$ and to ensure the solution's positive definiteness.

The polynomial $p(y, s)$ is not essential for certain positive RBFs, but a semipositive RBF should account for singularity. We evaluate the thin-plate spline's polynomial component as $p(y, s) = c_1(s) + c_2(s)y + c_3(s)x$ resolves 2D. The expansion coefficients in equation (8) must be orthogonal for RBF interpolation of the level set function. Other terms include

$$\sum_{i=1}^N \lambda_i(s) = \sum_{i=1}^N \lambda_i(s) y_i = \sum_{i=1}^N \lambda_i(s) x_i = 0. \quad (5)$$

Because of the function's constraints, it can be rewritten as a matrix.

$$G\alpha = f, \quad (6)$$

where $G = \begin{bmatrix} A & P \\ P^s & 0_{3 \times 3} \end{bmatrix}$, $A = \begin{bmatrix} g_1(y_1) & \cdots & g_N(y_1) \\ \vdots & \ddots & \vdots \\ g_1(y_N) & \cdots & g_N(y_N) \end{bmatrix}$,

$$P = \begin{bmatrix} 1 & y_1 & x_1 \\ \vdots & \vdots & \vdots \\ 1 & y_N & x_N \end{bmatrix} \alpha = [\lambda_1 \cdots \lambda_N \ c_1 \ c_2 \ c_3]^s$$

$$\text{and } f = [\Phi(y_1, s) \cdots \Phi(y_N, s) \ 0 \ 0 \ 0]^s.$$

3.7. Rapid and Accurate Image Super Resolution

3.7.1. Global Filter Learning. Use upscaled versions of the training database images that were initially, $x_i \in \mathbb{R}^{M \times n}$, with



FIGURE 2: Examples of images with their associated label.

TABLE 2: Dataset partition on fire and no fire.

Dataset	Training	Testing	Validation	Total
No fire	608	190	152	950
Fire	608	190	152	950
Total	1216	380	304	1900

TABLE 3: Improved dataset partition on augmentation.

Augmentation	Value
Rotation	$1^{\circ}\sim 50^{\circ}$
Translation	0.1~0.2
Shear transformation	0.1~0.2
Scaling	0.1~0.2

$i = 1, \dots, L$. To know more about the $d \times d$ filter h , the Euclidean distance between the collection's $\{x_i\}$ and desired HR training images $\{y_i\}$ are taken to minimise. Formally, this makes use of least squares and square minimization.

$$\min_h \sum_{i=1}^L \|B_i h - b_i\|_2^2, \quad (7)$$

where $h \in \mathbb{R}^{d^2}$. The filter in use is identified $h \in \mathbb{R}^{d \times d}$ when vectors are notated. $B_i \in \mathbb{R}^{MN \times d^2}$ consists of a matrix with patches of varying widths $d \times d$ and direct image extraction y_i , and rows of the matrix are generated for each patch. The vector $a_i \in \mathbb{R}^{MN}$ is made up of each pixel from y_i , corresponding to the patch center's overall coordinates, x_i .

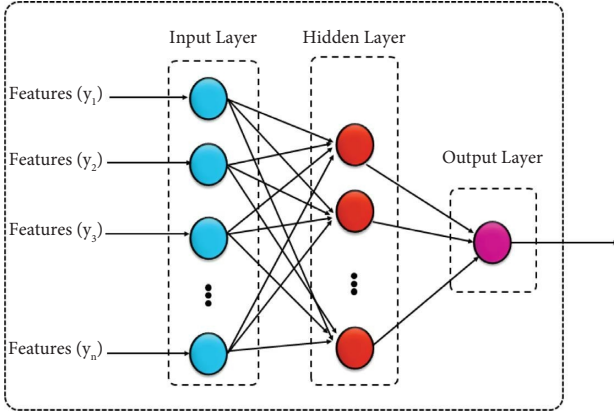


FIGURE 3: Structure of RBFN.

Figure 4 depicts the essential idea of the learning process as a block diagram.

Because A 's size may be prohibitive, we apply two strategies to reduce filter estimation calculation. To obtain an accurate estimate, it is optional to use every patch available. $K \ll MN$ patches/pixels are sampled from pictures on a predefined grid to produce A_i and b_i . Second, the least-squares minimization equation (7) can be modified to use the least amount of memory and computing resources possible. We will look into filter learning using just one image to keep things simple. It is simple to upload new photos and filters. For the learning phase, where the proposed approach excels, the memory size of the newly learned filter is ordered by size. To solve the problem, minimize equation (8).

$$\min_h \|Qh - V\|_2^2, \quad (8)$$

where

$$\begin{aligned} Q &= B^T B, \\ V &= B^T a. \end{aligned} \quad (9)$$

The vector V can be stored using a substantial similarity, which uses fewer bytes than the standard way of keeping the vector b . Furthermore, random access memory does not hold the complete matrix because of the fundamental features of matrix and matrix-vector multiplications. There are quantitative techniques for calculating Q , such as successively adding sets of rows.

This $B_j \in \mathbb{R}^{q \times d^2}$, ($q \ll MN$) can independently proliferate and then accumulate; this is what we understand by accumulation.

The multiplication of matrices and vectors yields the same result.

$$V = B^T a = \sum_j B_j^T a_j, \quad (10)$$

where $a_i \in \mathbb{R}^q$. By examining the vector b connected to the matrix, one can determine how much memory is required

for the suggested learning strategy approach which is minimal and equivalent to filter size. With the help of this realization, we may parallelize $B_j^T B_j$ and $B_j^T a_j$, to speed up the operation. If the matrix is semidefinite and has positive eigenvalues, then a quick conjugate gradient solver can determine the most negligible value of equation. Despite Q 's complexity, this is correct. During the learning phase, memory and parallelization efficiency are very high. We can approximate the high-resolution rendition of a low-resolution image not included in the training dataset by applying the same low-cost upscaling technique used during the learning process (such as bilinear interpolation) and filtering it with the previously acquired filter. Repeat this approach several times to achieve a reliable HR estimate.

3.8. Hashing-Based Learning and Upscaling. Global image filtering is the least expensive option because only one filter is applied to each pixel. Global filtering may improve the effectiveness of linear upscaling approaches for picture restoration by reducing the Euclidean distance between high-resolution and interpolated low-resolution images. Modern cutting-edge technologies, such as neural networks and sparsity, outperform the previously indicated global approach. The global technique's learning stage estimates the bare minimum of parameters without altering them based on the image content. Another disadvantage is the worldwide approach's complexity.

The best technique to customize a filter to the content of an image is to first cluster image patches. Patches are used for this. We wish to maintain the complexity of the clustering algorithm. In contrast to "expensive" clustering algorithms such as K-means, GMM, or dictionary learning, we propose a hashing approach that yields adaptive filtering with low complexity. Bucketing picture patches acquire local adaptability in line with a practical and cost-effective geometry metric that employs gradient statistics. We will then look at per-bucket filters, such as the global strategy. The proposed learning technique generates a filter hash table. Local gradient functions are the hash-table's keys, and learned filters are its contents.

Each patch is assigned a hash-table key, which is used to decide which of the four filters (one for each type of patch) should be applied to it. Each quantized edge-statistic descriptor's hash-filters table performs well for upscaling. We use matrix-matrix and matrix-vector multiplications in a similar way in global learning. To train a filter, we use q to reduce each bucket's cost function.

$$\min_{h_q} \|B_q^T B_q h_q - B_q^T a_q\|_2^2, \quad (11)$$

where B_q and $b_q a_q$ are the pixel and patch contents of the q -this folder. A large hash table with millions of samples can be used with very little memory and still produce accurate filter estimation. Each subimage block has a submatrix element that we collect. As a result, a versatile learning strategy is created.

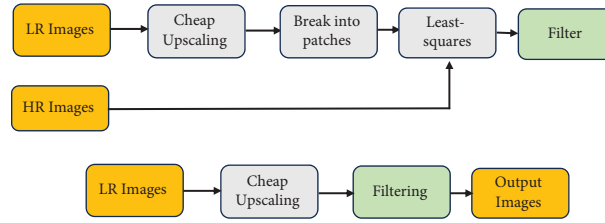


FIGURE 4: Structure of global filter learning.

3.9. *Hash-Table Keys: Local Gradient Statistics (Angle, Strength, and Coherence)*. Gradient statistics influence the suggested method. However, hash-table keys can be chosen from various local geometry metrics. Examine regional gradient features using eigen analysis. This displays the local consistency, gradient intensity, and gradient incline. Eigen analysis is useful when the neighborhood has a definite direction, but the average gradient is zero, as in thin lines or stripes. Smaller stripes and lines have more demand than larger ones. Signal strength, coherence, and direction can all be determined by $\sqrt{n} \times \sqrt{n}$. This entails taking into account all neighboring pixels for the k th pixel. k_1, \dots, k_n . The first step in the primary method is to generate a two-by- n matrix using the horizontal and vertical gradients, g_x and g_y , when k is the number of pixels surrounding the k th one, as indicated by

$$G_k = \begin{bmatrix} g_{x_{k1}} & g_{y_{k1}} \\ \vdots & \vdots \\ g_{x_{kn}} & g_{y_{kn}} \end{bmatrix}. \quad (12)$$

According to the study, this matrix's singular value decomposition can produce local gradient statistics (SVD). The two values in the equation stand in for the gradient's width and intensity, whereas the value on the right side indicates the gradient's orientation. Since we are working on a per-pixel basis, speed is crucial. Using an eigen decomposition of a two-by-two matrix constructed in a closed form may allow us to perform the computations for these features more quickly and with less computing power. In addition, we employ a separable normalized Gaussian kernel to construct a diagonal weighting matrix W_k , which allows us to include a limited neighborhood of gradient samples per pixel. As a result, we can aggregate a localized example of gradients. The largest eigenvalue of $G_k^T W_k G_k \phi_1^k$, related eigenvector ϕ_1^k , which is denoted by, can be used to calculate the gradient θ_k 's angle.

$$\theta_k = \arctan(\phi_{1,y}^k, \phi_{1,x}^k). \quad (13)$$

The symmetry ensures that a filter corresponding to angle k equals another filter corresponding to angle k . $\theta_k + 180^\circ = \arctan(\phi_{1,y}^k, \phi_{1,x}^k)$. The largest root square of the largest eigenvalue is shown in λ_1^k the gradient's "strength" Less-significant eigenvalue's square root λ_2^k can be thought of as the "spread" of regional gradients, or more precisely the extent to which their paths diverge from the beginning. The amount of power that each possesses can be used to

determine their level of control. The unitless metric coherence combines the two eigenvalues into a single value. The equation below determines the coherence value k , ranging between 0 and 1.

$$\mu_k = \frac{\sqrt{\lambda_1^k} - \sqrt{\lambda_2^k}}{\sqrt{\lambda_1^k} + \sqrt{\lambda_2^k}}. \quad (14)$$

The distinction of local visual features is enhanced by strength and coherence. A weak and incoherent signal indicates an image's lack of structure caused by noise or compression errors. Corners and multidirectionality are standard features of high-strength, low-coherence facilities. Coherence is characterized by solid stripes moving in the same direction. Picture semantics that is robust and consistent allows us to recognize location-dependent differences. To address these situations, filter learning uses the elements as hash components. Combining to create adaptive learning filters is demonstrated in Algorithm 1. Filters have several applications.

3.9.1. *Using Patch Symmetry for Nearly-Free 8x More Learning Examples*. Many data points may be required for filter set learning. To master a 9×9 or 11×11 filter, you must amass 105 patches. We can determine the number of patches needed for each B bucket. It takes more than 105 B patches using real-world training data to reach this amount. There is a system issue when some hash values are produced more frequently than others. The sky and painted surfaces are standard horizontal, vertical, and flat picture features. It stands to reason that these hashes are the most popular. This should help with the patches. It is possible to create eight sample patches, including four 90-degree and four mirror-image rotations. We can learn eight times as much since each patch generates eight more patches.

Transformed patches are mirrored and rotated to have their hash bucket and shift. The patch turns the hash bucket 90 degrees. It is worthless, given how expensive it is to change the aesthetic for each patch. Change patches may accumulate if gradient-angle-dependent hash bucket borders are symmetric to x -swaps, y -swaps, and xy -swaps. This symmetry's viability is established by hashing. We could accomplish this by using angle buckets evenly divided by four. Symmetry-augmented permuted matrices can be generated using symmetry. There are numerous approaches to this.

Inputs (1): Initial interpolated version of the LR image.
 (2): Q_θ -Quantization factor for angle (e.g. 24).
 (3): Q_s -Quantization factor for strength (e.g. 3).
 (4): Q_μ -Quantization factor for coherence (e.g. 3).
 Output
 (1): Hash-table keys per pixel, denoted by θ_k , λ_1^k , and μ_k .
 Process (i) Compute the image gradients
 (ii) Construct the matrix $G_k^T W_k G_k$, and obtain the gradients' angle θ_k , strength λ_1^k , and coherence μ_k
 (iii) Quantize: $\theta_1 \leftarrow \lceil \theta_i / Q_\theta \rceil$, $\lambda_1^i \leftarrow \lceil \lambda_1^i / Q_s \rceil$, $\mu_i \leftarrow \lceil \mu_i / Q_\mu \rceil$, where $\lceil \cdot \rceil$ is the ceiling function

ALGORITHM 1: Computing the hash-table keys.

The extra accumulation step needed for symmetry only takes up a tiny fraction of the learning time—less than 0.1%.

3.9.2. Compression and Sharpening Suppression of Artifacts. Blur and decimation are not common in practice, but the linear degradation model assumes them. Images are frequently noisy, compressed, postprocessed (such as with gamma correction), and distorted with an unknown kernel. RAISR can learn a reliable mapping for nonlinear degradation models. It is doable. Compression artifacts can be eliminated by learning a mapping from low-resolution photos that have been compressed to high-resolution images that have not been compressed. The compression parameter's bit rate or quality may affect the learning strategy. The quality level parameter JPEG encoders use has a scale from 0 (the lowest rate) to 100 (the best quality).

According to our findings, a more aggressive compression setting (such as 80) resulted in fewer compression artifacts and a smoother output. Using a moderate compression setting in training reduces compression artifacts and aliasing. This was discovered while attempting to minimize compression artifacts. Mapping LR training photos to sharpened HR copies of the same images can accomplish sharpening. RAISR upscaling produces more precise results as training progresses. We only use the prelearned filters during runtime. This is significant that because sharpening and compression are preprocessing operations, a compressed LR image can be mapped to a sharpened HR image using the learned filters. RAISR estimates missing spatial information, minimizes compression artifacts, and improves the signal. RAISR chooses this.

3.9.3. Blending: An Efficient Solution for Structure Preservation. The suggested learning system offers upscaling filters tailored to the provided image to reduce compression artifacts and increase image clarity. Sharpening increases noise and produces haloes around the edges. Both make mention of the sharpening process. The sharpening effect of learned filters can modify the structure of an interpolated image. To adapt your mixing correctly, keeping an eye on how the local structure changes after filtering is crucial. As a result, no significant structural adjustments are required.

When the structure of the filtered image is comparable to that of the interpolated image, we use it. We use the original, more extensive version of the image in locations where the filtering affects the image. This strategy takes advantage of the fact that interpolated images perform well in low-frequency zones despite being less expensive (e.g., flat regions). More attention is required when applying expected filters to higher spatial frequencies. The blending method considers both the upsampled and RAISR-filtered images. The idea's implementation would have been significantly slowed if clustering had been used to identify these locations. Here is a quick fix for point-wise blending involving two final photos.

The CT descriptor is recommended for identifying structural deformations and correcting upscaling errors. CT sparked this notion. The CT is summarised below to clarify the concept of mixing. A little (3×3) square of pixel intensity data is translated into a bit string that depicts a picture using this transformation. The CT is computed by rating intensity values received from different sites.

In contrast to standard SISR algorithms, the principal blending mechanism only increases the signal's high-frequency components. There is no need to improve the outcomes in these areas because there is no lost detail or aliasing after a linear upscale. Prelearned filters are essential due to linear interpolation's inability to recover ordered regions. Prelearned filters can produce haloes in well-organized areas, particularly near pronounced borders. Sharpening and the 1111 or 99-pixel filter size are two issues. Because the CT is not light-sensitive, we will see how magnifying only high-frequency picture components enables it to recognize edges and structures. Because CT is indifferent about the source of the morning, it cannot notice it.

The blend of weights results from "randomness," defined as the likelihood of finding a pixel inside a predetermined zone. The LCC and the overall strength and quantity of the structure are determined by the relevance in the CT descriptor window. The mass of an LCC increases in proportion to its volume. Identify whether a pixel represents an edge is feasible by studying its "randomness" in terms of the bit string that makes up the blending weights map. Only high frequencies benefit from the upscaling scheme's sharpness. This approach amplifies only higher frequencies.

- (i) SISR HR pictures can be improved by increasing the contrast or raising the low, mid, and high frequencies. A second CT-based mixing method might be advantageous.
- (ii) We did this to see how the local structure changed.
- (iii) Upscale and filter the pictures before computing the CT.
- (iv) The changed bits for each pixel must be determined. As the Hamming distance rises, so does the size of the structural shift.

The needed blending map can be generated by translating the adjusted bits into weights. CT is unaffected by measured intensity. Instead of employing randomness, this blending map minimizes structural change while allowing for local intensity adjustments (or contrast).

- (i) The recommended DoG sharpener executes HR target image preprocessing during learning. This enhances contrast and sharpens structures. Because the augmentation is built in, the prelearned filters improve high-frequency features and mid-to-low-frequency contrast. The scaling method enhances contrast.
- (ii) Our research shows that we can make photos with the same contrast as LR appears more realistic. When RAISR raises a more extensive range of frequencies (allowing for contrast modification), it generates better images, but the result may not be as excellent as LR's. If we improve the contrast, sharpen the image, and remove compression artifacts, our PSNR or SSIM comparisons will be less visible. Even though the photos appear excellent (much better than the originals!), this quantitative metric shows a deterioration.
- (iii) A low-resolution image is converted to a high-resolution image using the RAISR approach. The following are the procedure steps.
- (iv) Bilinear interpolation is used to scale up LR images.
- (v) A training database's filters in a hash table. Hash tables have filters, and their keys are gradient properties. Filters improve the output standard of step 1.
- (vi) The ultimate result is achieved by selectively combining steps I and (ii), wherein individual pixels are assigned unique weights.

4. Result and Discussion

4.1. Experimental Setup. This computer system was used to develop and evaluate object detection models. It had a 64 GB RAM chip, a 2 TB hard drive, and an 8-core Intel i7 9700 k processor. PyTorch (v1.7.1), torchvision (v0.8.2), OpenCV-python (v4.4.0.46), Detectron2 (v0.3), Albumentations (v0.5.2), and NumPy were among the Python software packages that were of significant value. It was running on Ubuntu 18.0.5.

4.2. Evaluation Metrics

- (i) True positives (TPs): instances where the actual yield and our expectations came true
- (ii) True negatives (TNs): occurrences where the real gain also turned out to be false, as we had predicted
- (iii) False positives (FPs): when we expected accurate results, the work was incorrect
- (iv) False negatives (FNs): when a result that we expected to be false turns out to be true

4.2.1. Accuracy. The positive rate is the percentage of times the hypothesis was proven correct. This is how we would quantify it:

$$\text{accuracy} = \frac{\text{TP}}{\text{TP} + \text{TN} + \text{FP} + \text{FN}}. \quad (15)$$

4.2.2. Recall. The following equation depicts a metric for evaluating the success of a favorable prognosis:

$$\text{recall} = \frac{\text{TP}}{\text{TP} + \text{FN}}. \quad (16)$$

4.2.3. Precision. Precision is a measure of accuracy and an equation that predicts how accurate an optimistic prediction is as follows:

$$\text{precision} = \frac{\text{TP}}{\text{TP} + \text{FP}}. \quad (17)$$

4.2.4. F-Score. There is a catch-22 situation with recall and precision. The metric is described as follows:

$$F - \text{score} = 2 \frac{\text{precision} * \text{recall}}{\text{precision} + \text{recall}}. \quad (18)$$

4.2.5. Root Mean Squared Error. It is the same as MSE; the only addition is a square root sign. The formula for mean absolute error is represented as follows:

$$\text{RMSE} = \sqrt{\sum_{i=1}^n \frac{(\hat{y}_i - y_i)^2}{n}}. \quad (19)$$

Root mean squared error (RMSE) takes the values from 0 to ∞ , and the smaller RMSE values are desirable.

4.2.6. Precision. Figure 5 and Table 4 demonstrate a precision comparison of the RBFN-RAISR methodology to other currently used methods. The graph depicts how the deep-learning approach has improved precision. When using data 100, for example, the RBFN-RAISR model has a precision value of 91.67%, while the CNN, R-CNN, SVM, ANN, DT, and BNN models have precision values of

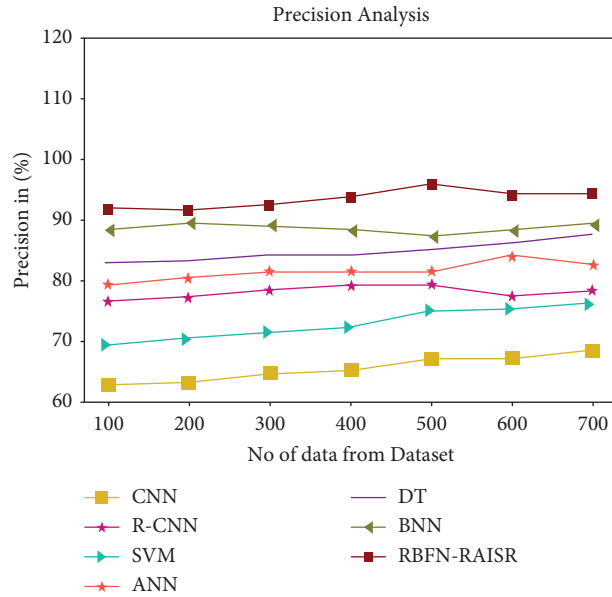


FIGURE 5: Precision analysis for the RBFN-RAISR technique with existing systems.

TABLE 4: Precision analysis for RBFN-RAISR technique with existing systems.

No. of data from dataset	CNN	R-CNN	SVM	ANN	DT	BNN	RBFN-RAISR
100	62.78	76.45	69.23	79.34	82.98	88.19	91.67
200	63.19	77.13	70.32	80.45	83.19	89.43	91.45
300	64.55	78.34	71.32	81.32	84.23	89.12	92.19
400	65.19	79.13	72.19	81.45	84.19	88.13	93.56
500	66.98	79.19	74.89	81.55	85.12	87.23	95.87
600	67.12	77.23	75.19	83.98	86.14	88.45	94.11
700	68.33	78.12	76.12	82.44	87.45	89.17	94.19

62.78%, 76.45%, 69.23%, 79.34%, 82.98%, and 88.19%, respectively. The RBFN-RAISR model, on the other hand, has demonstrated peak performance across a wide range of data sizes. Similar to this, the RBFN-RAISR model has a precision value of 94.19% when there are 700 data points, compared to precision values of 68.33%, 78.12%, 76.12%, 82.44%, 87.45%, and 89.17% for the CNN, R-CNN, SVM, ANN, DT, and BNN models.

4.2.7. Recall. Figure 6 and Table 5 show that the RBFN-RAISR recall is compared to existing techniques. Deep learning, as shown in the graph, has improved recall values. In comparison to CNN, R-CNN, SVM, ANN, DT, and BNN models, which have recall values of 71.65%, 75.12%, 78.13%, 80.23%, 84.98%, and 87.11%, respectively, RBFN-RAISR with data 100 has a recall of 92.98%. Large datasets provide better performance for the RBFN-RAISR model. The recall values of the CNN, R-CNN, SVM, ANN, DT, and BNN models are 74.55%, 77.33%, 76.12%, 79.67%, 82.77%, 86.34%, and 91.55%, respectively, while it is 96.44% for the RBFN-RAISR model.

4.2.8. F-Score. Figure 7 and Table 6 show that the RBFN-RAISR technique's F -score is tabulated compared to other methods. As shown in the graph, deep learning has enhanced f -score performance. According to data 100, RBFN-RAISR has an f -score of 87.34%, while CNN, R-CNN, SVM, ANN, DT, and BNN have f -scores of 51.89%, 57.45%, 60.34%, 66.34%, 73.34%, and 80.56%, respectively. Large data sets are optimal for the RBFN-RAISR model's improved performance. When there are 700 observations, the RBFN RAISR's f -score is 93.33%, whereas, for CNN, R-CNN, SVM, ANN, DT, and BNN, it is 56.77%, 60.22%, 65.56%, 72.89%, 79.22%, and 86.12%, respectively.

4.2.9. Accuracy. The analysis comparing the RBFN-RAISR approach's accuracy to that of other currently employed methods is presented in Figure 8 and Table 7. The graph depicts how the deep-learning approach has an improved accuracy performance. When using data 100, the accuracy value for the RBFN-RAISR model is 91.87%, while accuracy values for the CNN, R-CNN, SVM, ANN, DT, and BNN models are 61.89%, 73.98%, 68.12%, 82.56%, 79.34%, and 86.31%, respectively. The RBFN-RAISR model, on the other

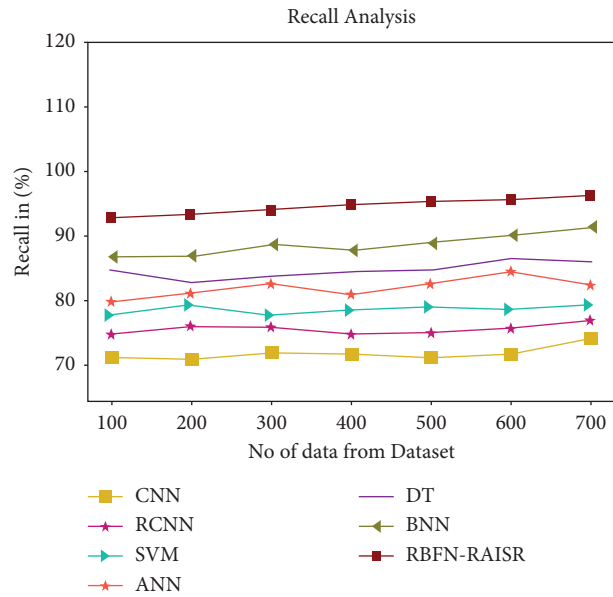


FIGURE 6: Recall analysis for the RBFN-RAISR technique with existing systems.

TABLE 5: Recall analysis for the RBFN-RAISR technique with existing systems.

No. of data from dataset	CNN	R-CNN	SVM	ANN	DT	BNN	RBFN-RAISR
100	71.65	75.12	78.13	80.23	84.98	87.11	92.98
200	71.45	76.45	79.56	81.56	83.12	87.34	93.45
300	72.33	76.34	78.12	82.91	84.22	88.97	94.12
400	72.19	75.19	78.87	81.22	84.77	88.13	94.89
500	71.67	75.44	79.33	82.98	85.12	89.34	95.55
600	72.19	76.12	79.12	84.88	86.67	90.45	95.78
700	74.55	77.33	79.67	82.77	86.34	91.55	96.44

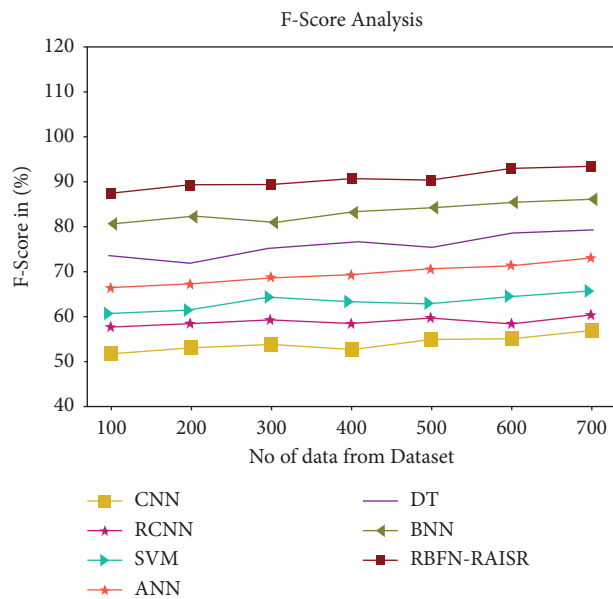


FIGURE 7: F-score analysis for the RBFN-RAISR technique with existing systems.

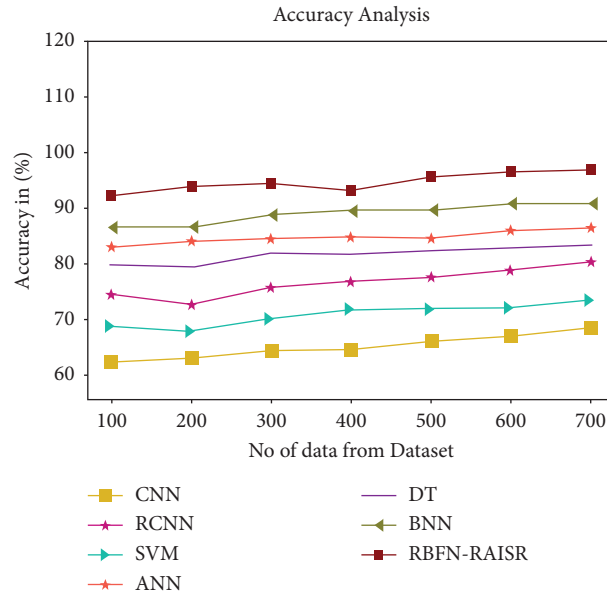


FIGURE 8: Accuracy analysis for the RBFN-RAISR technique with existing systems.

TABLE 6: F-score analysis for RBFN-RAISR technique with existing systems.

No. of data from dataset	CNN	R-CNN	SVM	ANN	DT	BNN	RBFN-RAISR
100	51.89	57.45	60.34	66.34	73.34	80.56	87.34
200	52.98	58.34	61.23	67.12	71.67	82.23	89.23
300	53.98	59.12	63.98	68.34	75.12	80.78	89.21
400	52.76	58.34	63.19	69.21	76.56	83.19	90.43
500	54.98	59.55	62.67	70.45	75.12	84.12	90.23
600	55.12	58.23	64.12	71.23	78.34	85.33	92.78
700	56.77	60.22	65.56	72.89	79.22	86.12	93.33

TABLE 7: Accuracy analysis for the RBFN-RAISR technique with existing systems.

No. of data from dataset	CNN	R-CNN	SVM	ANN	DT	BNN	RBFN-RAISR
100	61.89	73.98	68.12	82.56	79.34	86.31	91.87
200	62.56	72.12	67.34	83.78	78.98	86.34	93.65
300	63.98	75.34	69.56	84.12	81.56	88.45	94.12
400	64.12	76.34	71.22	84.45	81.24	89.12	94.87
500	65.55	77.12	71.45	84.23	81.89	89.45	95.34
600	66.45	78.45	71.67	85.67	82.45	90.48	96.12
700	67.98	79.89	72.89	86.13	82.87	90.56	97.55

hand, has demonstrated peak performance across a wide range of data sizes. The accuracy of the RBFN-RAISR model under 700 data points is 97.55%, whereas the accuracy of the CNN, R-CNN, SVM, ANN, DT, and BNN models is 67.98%, 79.89%, 72.89%, 86.13%, 82.87%, and 90.56%, respectively.

4.2.10. RMSE. Figure 9 and Table 8 show RMSE analyses of the RBFN-RAISR methodology compared to other methods. The data in the figure show that the deep learning strategy's

application improved performance with reduced RMSE values. Using data 100, the RMSE value for the RBFN-RAISR is calculated to be 21.89%, while CNN, R-CNN, SVM, ANN, DT, and BNN models have produced slightly higher RMSE values of 51.23%, 46.78%, 39.32%, 40.89%, 34.78%, and 32.89%, respectively. The RBFN-RAISR model, on the other hand, performs at its peak while maintaining low RMSE values across a wide range of data sizes. Similarly, the RMSE for the RBFN-RAISR model under 700 data points is 24.89 percent, whereas the RMSE values for CNN, R-CNN, SVM,

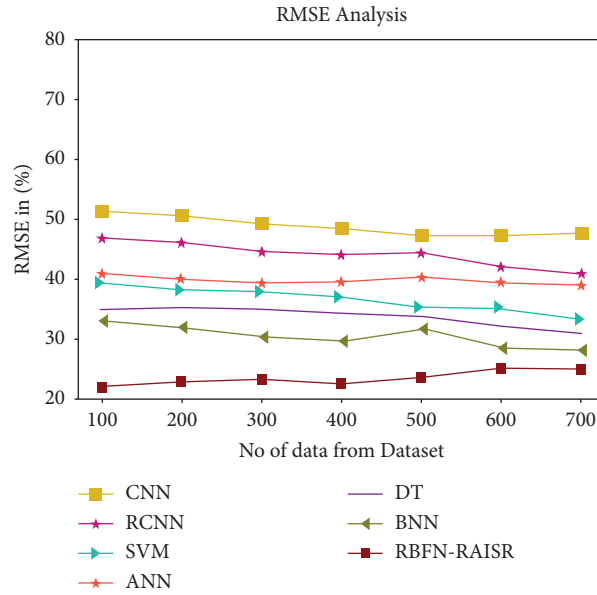


FIGURE 9: RMSE analysis for the RBFN-RAISR technique with existing systems.

TABLE 8: RMSE analysis for the RBFN-RAISR technique with existing systems.

No. of data from dataset	CNN	R-CNN	SVM	ANN	DT	BNN	RBFN-RAISR
100	51.23	46.78	39.32	40.89	34.78	32.89	21.89
200	50.56	45.99	38.12	39.87	35.12	31.87	22.78
300	49.23	44.45	37.66	39.21	34.98	30.21	23.19
400	48.44	43.98	36.98	39.45	34.18	29.67	22.44
500	47.12	44.34	35.12	40.21	33.66	31.67	23.55
600	47.33	41.98	34.98	39.45	32.12	28.56	25.12
700	47.55	40.77	33.11	38.89	30.87	28.11	24.89

TABLE 9: Execution time analysis for the RBFN-RAISR method with existing systems.

No. of data from dataset	CNN	R-CNN	SVM	ANN	DT	BNN	RBFN-RAISR
100	6.432	5.345	8.543	8.154	3.213	5.453	1.672
200	6.187	5.167	8.123	8.432	3.987	5.765	1.876
300	6.321	6.987	8.567	8.132	3.876	5.125	1.987
400	7.987	6.123	8.543	9.765	4.432	5.987	2.675
500	7.543	6.453	8.987	9.654	4.123	5.197	2.765
600	7.865	6.876	9.675	9.134	4.876	5.123	2.876
700	7.432	6.987	9.765	9.567	5.123	4.654	2.234

ANN, DT, and BNN models are 47.55%, 40.77%, 33.11%, 38.89%, 30.87%, and 28.11%, respectively.

4.2.11. Execution Time. Table 9 and Figure 10 compare how long the RBFN-RAISR methodology takes to execute compared to other methods. The results show that the RBFN-RAISR method outperformed all the different

techniques. For example, the RBFN-RAISR process with 100 data takes only 1.672 seconds to run, whereas the execution times of other existing methods such as CNN, R-CNN, SVM, ANN, DT, and BNN are 6.432 sec, 5.345 sec, 8.543 sec, 8.154 sec, and 3.213 seconds, respectively. In a similar vein, the RBFN-RAISR approach takes only 2.234 seconds to run on 700 data, compared to 7.432 seconds, 6.987 seconds,

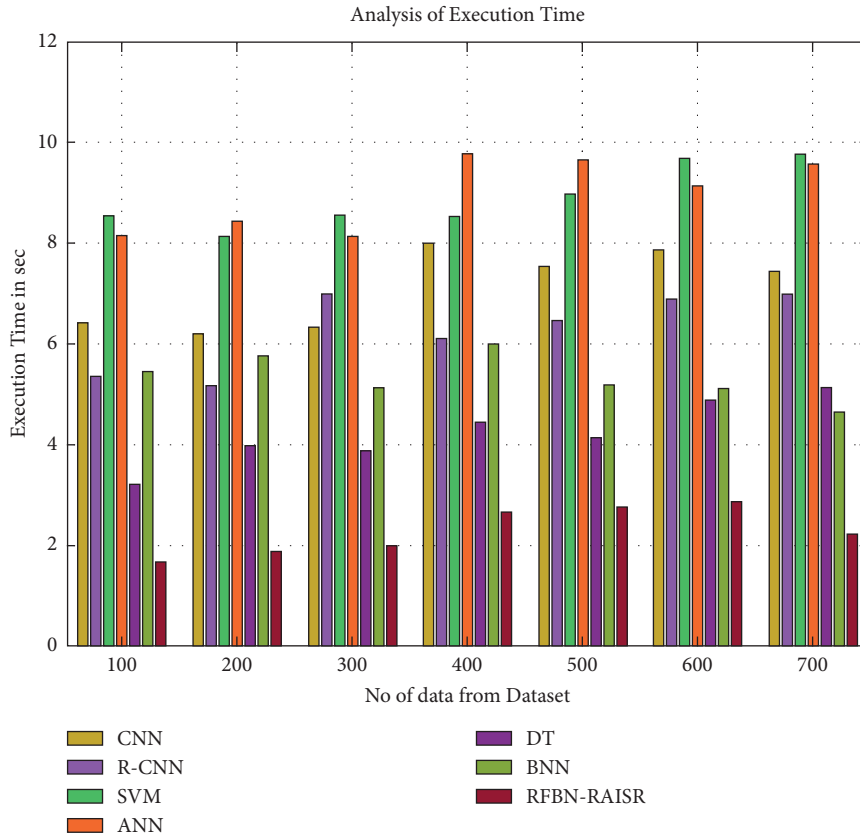


FIGURE 10: Execution time analysis for the RBFN-RAISR method with existing systems.

9.765 seconds, 9.567 seconds, 5.123 seconds, and 4.654 seconds for the other methods currently in use, such as CNN, R-CNN, SVM, ANN, DT, and BNN, respectively.

5. Conclusion

The primary focus of this work is a deep learning-based early warning system for detecting forest fires. Forest fires have recently become a significant problem as a result of climatic changes that are both natural and anthropogenic. We devised an artificial intelligence-based system for detecting forest fires to stop severe disasters and notice them early. This paper comprehensively explains vision-based methods for classifying and localizing forest fires. The dataset from forest fire detection was also used to tackle the classification challenge of identifying fires in images. This study evaluates a manually created classifier for identifying and grouping images based on their likelihood of containing flames. The tests made use of aerial photographs with few fire pixels. Fire detection precision has improved. This technique uses datasets to train satellite images to distinguish between fire and other images. It employs transfer learning on the convolutional neural network-based Inception-v3 algorithm. Therefore, to prevent adverse effects, the automated identification of current forest fires (together with burning biomass) holds substantial importance as a study domain. Making decisions early on can assist decision-makers in planning mitigation and extinguishment strategies. Radial

basis function networks (RBFNs) with RAISR is a deep-learning framework trained on an input dataset to detect active fires and burning biomass. The proposed RBFN-RAISR model's performance in recognizing fires and non-fires was evaluated using a variety of performance metrics and compared to previous CNN models. The water wave optimization technique is used for effective picture feature selection, image noise, blurring reduction, and image enhancement and restoration. In this method existing models such as CNN, R-CNN, SVM, ANN, DT, and BNN were discovered. When attempting to determine whether or not a user belongs to a specific category, the proposed model produces the best results (an overall accuracy of 97.55%), with prediction performance being relatively insensitive to model selection. To increase the accuracy, interpretability, and robustness of wildfire image detection and classification systems for effective biomass control, combining deep learning techniques with other methods, such as sensor networks, physical models, or strategies based on domain knowledge, is frequently necessary. This is due to the limitations of the proposed methods. The images in the collection of forest fire detection photos will have their spatial resolution enhanced in further study. A cutting-edge photo segmentation system utilizing CNN technology is being created to overcome the difficulties in locating forest fires. To improve the dependability of fire detection systems, the main goal is to reduce the incidence of false alarms drastically.

Data Availability

The data used to support the findings of this study are available from the corresponding author upon request.

Conflicts of Interest

The authors declare that there are no conflicts of interest.

References

- [1] K. B. Bhujel, R. Maskey-Byanju, and A. P. Gautam, "Wildfire dynamics in Nepal from 2000–2016," *Nepal Journal of Environmental Science*, vol. 5, pp. 1–8, 2017.
- [2] A. Mannan, Z. Feng, A. Ahmad et al., "CO2 emission trends and risk zone mapping of forest fires in subtropical and moist temperate forests of Pakistan," *Applied Ecology and Environmental Research*, vol. 17, no. 2, pp. 2983–3002, 2019.
- [3] R. H. Nolan, M. M. Boer, L. Collins et al., "Causes and consequences of eastern Australia's 2019-20 season of mega-fires," *Global Change Biology*, vol. 26, no. 3, pp. 1039–1041, 2020.
- [4] Z. Guan, F. Min, W. He, W. Fang, and T. Lu, "Forest fire detection via feature entropy guided neural network," *Entropy*, vol. 24, no. 1, p. 128, 2022.
- [5] C. Maxouris, "Here's just how bad the devastating Australian fires are—by the numbers," 2021, <https://edition.cnn.com/2020/01/06/us/australian-fires-by-the-numbers-trnd/index.html>.
- [6] State of California, "Thomas fire incident information," 2021, <https://fire.ca.gov/incident/?incident=d28bc34e-73a8-454d-9e55-dea7bdd40bee>.
- [7] M. Rodrigues, P. J. Gelabert, A. Ameztegui, L. Coll, and C. Vega-Garcia, "Has COVID-19 halted winter-spring wildfires in the mediterranean? Insights for wild-fire science under a pandemic context," *The Science of the Total Environment*, vol. 765, Article ID 142793, 2021.
- [8] Y. Kountouris, "Human activity, daylight saving time and wildfire occurrence," *The Science of the Total Environment*, vol. 727, Article ID 138044, 2020.
- [9] T. Kim, C. Ramos, and S. Mohammed, "Smart city and IoT," *Future Generation Computer Systems*, vol. 76, pp. 159–162, 2017.
- [10] Y. C. Hsiao, M. H. Wu, and S. C. Li, "Elevated performance of the smart city—a case study of the IoT by innovation mode," *IEEE Transactions on Engineering Management*, vol. 68, no. 5, pp. 1461–1475, 2021.
- [11] V. Chowdary, M. K. Gupta, and R. Singh, "A Review on forest fire detection techniques: a decadal perspective," *Networks*, vol. 4, p. 12, 2018.
- [12] K. Bot and J. G. Borges, "A systematic review of applications of machine learning techniques for wildfire management decision support," *Inventions*, vol. 7, no. 1, p. 15, 2022.
- [13] A. Khan, S. Khan, B. Hassan, and Z. Zheng, "CNN-based smoker classification and detection in smart city application," *Sensors*, vol. 22, no. 3, p. 892, 2022.
- [14] S. Neelakandan, D. Paulraj, P. Ezhumalai, and M. Prakash, "A Deep Learning Modified Neural Network (DLMNN) based proficient sentiment analysis technique on Twitter data," *Journal of Experimental & Theoretical Artificial Intelligence*, pp. 1–20, 2022.
- [15] A. Bouguettaya, H. Zarzour, A. M. Taberkit, and A. Kechida, "A review on early wildfire detection from unmanned aerial vehicles using deep learning-based computer vision algorithms," *Signal Processing*, vol. 190, Article ID 108309, 2022.
- [16] Y. Cao, F. Yang, Q. Tang, and X. Lu, "An attention enhanced bidirectional LSTM for early forest fire smoke recognition," *IEEE Access*, vol. 7, pp. 154732–154742, 2019.
- [17] M. J. Sousa, A. Moutinho, and M. Almeida, "Wildfire detection using transfer learning on augmented datasets," *Expert Systems with Applications*, vol. 142, Article ID 112975, 2020.
- [18] D. Alexandrov, E. Pertseva, I. Berman, I. Pantiukhin, and A. Kapitonov, "Analysis of machine learning methods for wildfire security monitoring with an unmanned aerial vehicles," in *Proceedings of the 24th Conference of Open Innovations Association FRUCT (Finnish-Russian University Cooperation in Telecommunications)*, pp. 3–9, Moscow, Russia, April 2019.
- [19] Q. Zhang, J. Xu, L. Xu, and H. Guo, "Deep convolutional neural networks for forest fire detection," in *Proceedings of the International Forum on Management, Education and Information Technology Application*, Y. H. Kim, Ed., pp. 568–575, Atlantis Press, Guangzhou, China, January 2016.
- [20] H. Yar, T. Hussain, M. Agarwal, Z. A. Khan, S. K. Gupta, and S. W. Baik, "Optimized dual fire attention network and medium-scale fire classification benchmark," *IEEE Transactions on Image Processing*, vol. 31, pp. 6331–6343, 2022.
- [21] S. N. Saydirasulovich, A. Abdusalomov, M. K. Jamil, R. Nasimov, D. Kozhamzharova, and Y.-I. Cho, "A YOLOv6-based improved fire detection approach for smart city environments," *Sensors*, vol. 23, no. 6, p. 3161, 2023.
- [22] H. Yar, T. Hussain, Z. A. Khan, D. Koundal, M. Y. Lee, and S. W. Baik, "Vision sensor-based real-time fire detection in resource-constrained IoT environments," *Computational Intelligence and Neuroscience*, vol. 2021, Article ID 5195508, 15 pages, 2021.
- [23] Y. O. Sayad, H. Mousannif, and H. Al Moatassime, "Predictive modeling of wildfires: a new dataset and machine learning approach," *Fire Safety Journal*, vol. 104, pp. 130–146, 2019.
- [24] Z. A. Khan, T. Hussain, F. U. M. Ullah, S. K. Gupta, M. Y. Lee, and S. W. Baik, "Randomly initialized CNN with densely connected stacked autoencoder for efficient fire detection," *Engineering Applications of Artificial Intelligence*, vol. 116, Article ID 105403, 2022.
- [25] Q. X. Zhang, G. H. Lin, Y. M. Zhang, G. Xu, and J. J. Wang, "Wildland forest fire smoke detection based on faster R-CNN using synthetic smoke images," *Procedia Engineering*, vol. 211, pp. 441–446, 2018.
- [26] A. Khan, B. Hassan, S. Khan, R. Ahmed, and A. Abuassba, "DeepFire: a novel dataset and deep transfer learning benchmark for forest fire detection," *Mobile Information Systems*, vol. 2022, Article ID 5358359, 14 pages, 2022.
- [27] M. Park, D. Q. Tran, S. Lee, and S. Park, "Multilabel image classification with deep transfer learning for decision support on wildfire response," *Remote Sensing*, vol. 13, no. 19, p. 3985, 2021.
- [28] R. Kaabi, M. Sayadi, M. Bouchouicha, F. Fnaiech, E. Moreau, and J. M. Ginoux, "Early smoke detection of forest wildfire video using deep belief network," in *Proceedings of the International Conference on Advanced Technologies for Signal and Image Processing (ATSIP)*, pp. 1–6, Sousse, Tunisia, March 2018.
- [29] Y. Tang, H. Feng, J. Chen, and Y. Chen, "A deep learning algorithm for forest image classification," in *Proceedings of the 2nd International Conference on Computer Vision and Data Mining*, Changsha, China, August 2021.

- [30] W. Li and Z. Yu, "A lightweight convolutional neural network flame detection algorithm," in *Proceedings of the IEEE International Conference on Electronics Information and Emergency Communication (ICEIEC)*, pp. 83–86, Beijing, China, June 2021.
- [31] Kaggle, "Forest fire dataset," 2022, <https://www.kaggle.com/code/brsdincer/forest-fire-detection-prediction-all-process>.
- [32] E. Jang, Y. Kang, J. Im, D.-W. Lee, J. Yoon, and S.-K. Kim, "Detection and monitoring of forest fires using himawari-8 geostationary satellite data in South Korea," *Remote Sensing*, vol. 11, no. 3, p. 271, 2019.
- [33] C. Zhai, S. Zhang, Z. Cao, and X. Wang, "Learning-based prediction of wildfire spread with real-time rate of spread measurement," *Combustion and Flame*, vol. 215, pp. 333–341, 2020.
- [34] M. Koushki, E. Jabbari, and M. Ahmadiania, "Evaluating RBF methods for solving PDEs using Padua points distribution," *Alexandria Engineering Journal*, vol. 59, no. 5, pp. 2999–3018, 2020.
- [35] P. Wei, Z. Li, X. Li, and M. Y. Wang, "An 88-line MATLAB code for the parameterized level set method-based topology optimization using radial basis functions," *Structural and Multidisciplinary Optimization*, vol. 58, no. 2, pp. 831–849, 2018.